Real-Time Reconfiguration and Safe Navigation for AUVs Network using Distributed Nonlinear MPC and Relaxed CBFs: Theory and Experimental Validation

Minh Nhat Nguyen*, Stephen McIlvanna*, Jack Close*, Mien Van, and Charalampos C. Tsimenidis, *Senior Member, IEEE*

***Abstract*—The deployment of multiple Autonomous Underwater Vehicles (AUVs) is vital for achieving comprehensive cooperative missions and extensive spatial coverage. However, limited communication between agents necessitates a robust and distributed coordination strategy to maintain operational effectiveness and reliability. This study explores the design and implementation of a new distributed Nonlinear Model Predictive Control (NMPC) scheme that integrates Control Barrier Functions (CBFs) with a relaxed decay rate of the barrier function for trajectory tracking and formation control of multiple BlueRov2 underwater robots. Acting as safety constraints, CBFs guarantee system safety and performance objectives are simultaneously considered within a short prediction horizon, reducing the computational burden in real-time implementation. Additionally, the relaxed decay rate technique enhances the feasibility of the optimisation and system safety at the same time. The stability analysis of the closed-loop system is provided. A series of challenging scenarios, including obstacles, are conducted in the Software-in-the-loop (SITL) simulation, as well as the open sea and river environments, to demonstrate the robustness and flexibility of the proposed control strategy, guaranteeing safe and coordinated operations of multiple underwater robots.**

***Index Terms*—Underwater robot, Nonlinear Model Predictive Control, Control Barrier Function, Multiple Agents, BlueRov2.**

I. Introduction

Autonomous Underwater Vehicles (AUVs) are crucial for oceanographic research, underwater exploration, and environmental monitoring. They operate autonomously in hazardous underwater environments, performing tasks impractical for human divers or Remotely Operated Vehicles (ROVs). AUVs enable detailed ocean floor mapping, essential for understanding geological features and tectonic activities [1], and support long-term monitoring of oceanographic parameters crucial for climate change studies [2]. They also assess oil spill impacts, track harmful algal blooms, and monitor marine ecosystems [3]. The increasing reliance on AUVs across these diverse applications highlights the potential and necessity of deploying multiple AUVs in coordinated operations to enhance data collection efficiency and spatial coverage.

Various methods have been developed to address the challenges of coordination and control, enabling the maintenance of desired formations and the achievement of specific objectives in complex environments. The behavioural strategy designs individual behaviours for each agent to achieve desired group dynamics [4], [5]. The virtual structure scheme treats the entire formation as a cohesive entity, controlling its motion to maintain relative positions [6], [7]. Consensus-based approaches enable agents to agree on key state variables, such as position or velocity, through local interactions [8], [9]. Artificial potential-based techniques use potential fields to create attractive or repulsive forces among agents and obstacles, guiding the formation while preventing collisions [10], [11]. The leader-follower method designates specific agents as leaders to navigate, with followers adjusting their positions to maintain formation [12]- [14].

The leader-follower formation control method is widely recognised for its practicality and prevalence in the domain of formation control. In this approach, a team of AUVs can include one or multiple leaders. As the leader's posture changes, the followers determine the estimation errors of its displacement and direction through a combination of perception, calculation, and communication. Consequently, the control problem for the followers transforms into a point stabilisation task relative to the leader's pose, independent of the leader's dynamics. This is particularly advantageous for AUVs due to the low bandwidth, weak underwater communication, and low update rates [15]. For the leader's trajectory tracking control, various advanced methods have been developed to enhance the tracking accuracy and robustness of AUVs. Sliding Mode Control (SMC), including distributed bioinspired SMC [16] and terminal SMC [17], provides robust performance and adaptability, crucial for stability in uncertain underwater environments. Finite-time control strategies [18]- [20] ensure rapid convergence and accurate tracking for time-sensitive missions. Fixed-time control methods [12], [21], [22] address challenges like communication delays and system nonlinearities, offering consistent performance regardless of initial conditions. Neural

This work was supported by the DASA/DSTL ORCA project [grant number ACC6042115], and partly supported by the Natural Environment Research Council, United Kingdom [grant number NE/V008080/1] and by the Royal Society [grant number IEC/NSFC/211236 and grant number RGS/R1/221356]. (Corresponding author: Mien Van.)

Nhat Minh Nguyen, Stephen McIlvanna, Jack Close, and Mien Van are with the School of Electronics, Electrical Engineering and Computer Science, Queen's University Belfast, Belfast, UK (email: nnhat01@qub.ac.uk; smcilvanna01@qub.ac.uk; jclose06@qub.ac.uk; m.van@qub.ac.uk).

Charalampos C. Tsimenidis is with the Department of Engineering, School of Science and Technology, Nottingham Trent University, Nottingham NG1 4FQ, UK (email: charalampos.tsimenidis@ntu.ac.uk)

*These authors contributed equally to this work.

network-based approaches and reinforcement learning [23]-[25] incorporate adaptive learning, improving tracking accuracy and handling complex, unmodeled dynamics effectively. In addition to the advanced control approaches mentioned, NMPC emerges as a highly promising strategy for AUV tracking control due to its ability to handle multi-objective optimisation problems, which is crucial for complex underwater missions that require balancing multiple performance criteria such as energy efficiency, collision avoidance, and precise trajectory tracking. Another major advantage of NMPC is its capability to manage hard constraints for actuator saturations, communication range limitations, and safety issues. The adoption of NMPC for a single AUV in [26] - [28] and for multi-AUV systems in [29], [30] has proven to be a strategic advancement, leveraging predictive modelling and optimisation to navigate the challenges of underwater environments, ensuring robust, efficient, and adaptive performance. However, none of the NMPC schemes [27] - [30] explicitly considered obstacle avoidance ability for AUVs. NMPC in [26] integrated safety through predefined state and input constraints based on a static map of the environment, which includes fixed obstacles and workspace boundaries. However, this strategy may not be as effective in dynamic environments with moving obstacles due to its reliance on predefined constraints that may not adapt quickly to changes in the environment. CBFs are designed to rigorously enforce state constraints to adapt to changes [31], allowing the robot to dynamically adjust its path to avoid obstacles while considering real-time feedback. Additionally, the NMPC-CBF scheme can achieve comparable performance to traditional safety constraint approaches within a short prediction time, as in our previous work [32], which is beneficial for the limited computational resources of AUVs. Recent studies on new types of CBFs with a relaxed decay rate of the barrier function have shown potential to enhance both system safety and optimisation feasibility [33], [34].
In summary, there are existing research gaps in the reconfiguration and safe navigation of the multi-AUVs system:

1) Lack of investigation on integrating NMPC with CBF constraints for the safety-critical control of single or multi-AUV systems.
2) Notable absence of real-time reconfiguration and trajectory tracking verification for multi-agent systems.
3) Lack of validation for underwater robots in enhanced sea-state environments.
4) Lack of stability analysis for the NMPC-Relax-CBF scheme.

Motivated by the preceding analysis, this paper studies the leader-follower formation control problem of multiple AUVs (or underwater robots) where only one AUV knows the reference trajectory. Most of the aforementioned strategies require each robot to communicate with the entire team, which restricts the number of robots involved in the cooperative task and limits the team's spatial coverage. To overcome this limitation, a configuration of AUVs is proposed where the AUVs are interconnected to form a network, facilitating data transmission over extended distances. Two distributed NMPC schemes are designed for trajectory tracking and stabilisation problems. The proposed controllers are verified in the ArduPilot SITL simulation as an intermediate step before working with AUV hardware. Multiple challenging experimental setups, both with and without obstacles, are devised to evaluate the safety and formation control performance of the proposed approach. The main contributions of this manuscript are outlined as follows:

- A novel safety-critical control scheme integrates NMPC and CBF with a relaxed decay rate of the barrier function across the prediction horizon for the AUVs for the first time. This method can resolve the trade-off between feasibility and safety in Optimal Control Problems (OCP).
- A new distributed formation algorithm that uses a network of AUVs as relaying units to maximise the team's operational coverage. This algorithm incorporates a 6-DOF kinematic model of the AUV (e.g., BlueRov2), enabling full spatial manoeuvrability and precise orientation control for executing complex collaborative tasks.
- Several simulations in ArduPilot SITL, including obstacles, are set up to develop the proposed framework.
- Unlike all of the aforementioned papers [4] - [30], which verified proposed controllers only in simulation or indoor water tanks that may not consider environmental disturbances and practical issues, this study validates the proposed control strategy through real-time experiments. These experiments involve multiple BlueRov2 underwater robots in various challenging scenarios, including open sea and river environments.

The paper is organised as follows: Section 2 formulates the control problems for the AUV (i.e., BlueRov2). Section 3 covers the control approach, encompassing the development of NMPC, safety constraints, and proof of the stability of the closed-loop system. Section 4 presents experimental implementations, including a comparative analysis and discussion. Finally, Section 5 concludes the article.

II. Problem Formulation

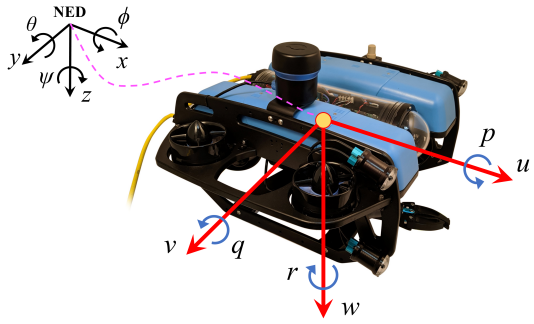

Fig. 1. The reference frames of the BlueRov2.

We study the coordinated motion control of a group of n AUV (i.e., BlueRov2). For each AUV $i \in \{1, ..., n\}$, its kinematic is described by a differential equation involving its position and velocity. In the i-th AUV, the position vector $\xi_i = [x_i, y_i, z_i, \phi_i, \theta_i, \psi_i]^T \in \Re^{6\times 1}$ represents the relative pose of the vehicle with respect to a fixed global reference system (NED). This vector includes the spatial coordinates of its body centre $\xi_{si} = [x_i, y_i, z_i]^T$ (m) and the orientation

angles $\xi_{oi} = [\phi_i, \theta_i, \psi_i]^T$ (rad) around the axes, as shown in Fig. 1. Meanwhile, the velocity of the i-th AUV is defined by the velocity vector, $\mathcal{V}_i = [u_i, v_i, w_i, p_i, q_i, r_i]^T \in \Re^{6\times 1}$. The directional velocities $\mathcal{V}_{di} = [u_i, v_i, w_i]^T$ (m/s) and the angular velocities $\mathcal{V}_{ai} = [p_i, q_i, r_i]^T$ (rad/s) represent the rate of turn around the x, y, and z axes. The relationship of the body frame velocity $\mathcal{V}_i$ and position ξ_i in the fixed global frame is:

$$\begin{aligned}\dot{\xi}_i(t) &= \mathbf{f}_i(\xi_i(t), \mathcal{V}_i(t)) \\ &= R(\xi_{oi}(t))\mathcal{V}_i(t)\end{aligned} \tag{1}$$

where $R(\xi_{oi}) \in \Re^{6\times 6}$ represents the coordinate transformation from the vehicle body frame to the NED reference frame.

$$R(\xi_{oi}) = \begin{bmatrix} R_1(\xi_{oi}) & 0^{3\times 3} \\ 0^{3\times 3} & R_2(\xi_{oi}) \end{bmatrix} \tag{2}$$

where the rotation matrix $R_1(\xi_{oi}) \in \Re^{3\times 3}$ is calculated as:

$$R_1(\xi_{oi}) = \begin{bmatrix} c\psi_i c\theta_i & c\psi_i s\theta_i s\phi_i - s\psi_i c\phi_i & c\psi_i c\phi_i s\theta_i + s\phi_i s\psi_i \\ s\psi_i c\theta_i & s\psi_i s\theta_i s\phi_i + c\psi_i c\phi_i & s\psi_i s\theta_i c\phi_i - c\psi_i s\phi_i \\ -s\theta_i & c\theta_i s\phi_i & c\theta_i c\phi_i \end{bmatrix} \tag{3}$$

and the angular transformation matrix $R_2(\xi_{oi}) \in \Re^{3\times 3}$

$$R_2(\xi_{oi}) = \begin{bmatrix} 1 & s\phi_i s\theta_i / c\theta_i & c\phi_i s\theta_i / c\theta_i \\ 0 & c\phi_i & -s\phi_i \\ 0 & s\phi_i / c\theta_i & c\phi_i / c\theta_i \end{bmatrix} \tag{4}$$

This study addresses two core control challenges: stabilisation and trajectory tracking. For stabilisation, the goal is a constant target pose ξ_r and a zero control vector $\mathcal{V}_r = 0_{6\times 1}$. In trajectory tracking, both ξ_r and $\mathcal{V}_r$ vary over time following a predetermined path. Both scenarios utilise a discretised kinematic model with a sampling period $\tau > 0$. Denoting $\xi(k) = \xi(t_k)$, the integration over the fixed interval is numerically approximated with a piecewise constant control during each sampling interval and the Runge-Kutta 4 (RK4) method.

$$\begin{aligned}\xi_i(k+1) &= \mathbf{F}_i(\xi_i(k), \mathcal{V}_i(k)) \\ &= \xi_i(k) + \int_{t_k}^{t_k+\tau} \mathbf{f}_i(\xi_i(t), \mathcal{V}_i(t))\, dt\end{aligned} \tag{5}$$

Denoting $k \in \mathbb{N}_0$ is the current sampling instant and $\mathbf{F}_i(\cdot) : \Re^6 \times \Re^6 \to \Re^6$ is the discrete nonlinear kinematic mapping of i-th AUV. In the stabilisation control problem, the feedback control is designed such that the solution of (5) starting from the initial condition $\xi_{0,i} := \xi_i(0) \in \mathbf{X}$ stays close to a desired set point, $\xi_{r,i} \in \mathbf{X}$, and converges, i.e.

$$\lim_{k\to\infty} \|\xi_{e,i}(k)\| = \lim_{k\to\infty} \|\xi_i(k) - \xi_{r,i}\| = 0 \tag{6}$$

In the trajectory control problem, the goal of the feedback control is to guide the solution of (5) to follow a time-varying reference such that

$$\lim_{k\to\infty} \|\xi_{e,i}(k)\| = \lim_{k\to\infty} \|\xi_i(k) - \xi_{r,i}(k)\| = 0 \tag{7}$$

III. Control Design

Consider n AUV agents operating in a workspace $W \subset \Re^3$. The team is organized into pairs of leaders and followers, forming $n-1$ decentralized subsystems, each consisting of two AUVs. In each subsystem, the follower AUV aims to maintain a specific distance and orientation relative to its leader. The formation is considered achieved when all AUVs reach their designated positions, as shown in Fig. 2 (a). The leader-follower formation problem is described as follows: Given the pose ξ_L of the leader vehicle, the follower's reference trajectory is determined by shifting its position by a distance d and angles $(\Delta\phi, \Delta\theta, \Delta\psi)$ relative to the leader. The follower's reference trajectory is continuously updated as the leader moves. This study employs a network of AUVs as relaying units to extend the operational coverage capacity of the team. In this network, only AUV1 receives the desired trajectory directly from a base computer. AUV1 then broadcasts its current state, denoted as ξ_1, and a formation vector, $\mathcal{A} = [\Delta x, \Delta y, \Delta z, \Delta\phi, \Delta\theta, \Delta\psi]^T$, to its follower. This process is sequentially continued until the last agent, with AUV3 receiving information from AUV2, as illustrated in Fig. 2 (b).

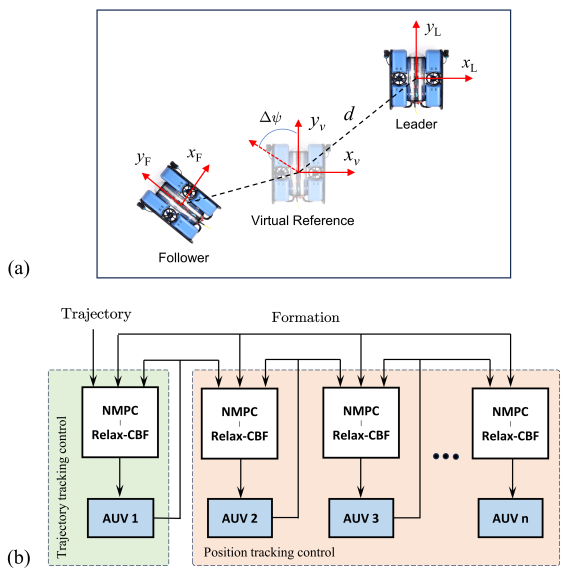

Fig. 2. A pair of leader-follower formation.

A. Proximity Graph

The communication structure among the AUV team is represented by a dynamic proximity graph $\mathcal{G} = (H, E(t))$. Here, H signifies the set of vertices corresponding to each AUV i in the team, $i \in 1, \ldots, n$. The edge set $E(t)$ at time step t_k reflects the existing communication links between AUVs if the Euclidean distance between their positions $\xi_{s,i}(t)$ and $\xi_{s,j}(t)$ is within communication range $\mathcal{C}$. Thus, $E(t)$ is defined by

$$E(t) = \{(i,j) \mid \|\xi_{s,i}(t) - \xi_{s,j}(t)\| \le \mathcal{C}, \forall i, j \in H, i \neq j\} \tag{8}$$

At any time t, a pair of AUVs (i,j) are considered neighbours if they are connected by an edge in $E(t)$, and the set of neigh-

bours for each AUV i is defined as $\mathcal{N}_i(t) = \{j|(i,j) \in E(t)\}$. Notably, the configuration of the proximity graph $\mathcal{G}$ changes dynamically as AUVs move within the workspace, altering both $E(t)$ and $\mathcal{N}_i(t)$.

B. Control Barrier Function

Definition 1. Let $\mathbb{R}_{\geq 0}$ denotes the non-negative real. A function $\alpha : \mathbb{R}_{\geq 0} \to \mathbb{R}_{\geq 0}$ is a class $\mathcal{K}$-function if it is continuous, strictly increasing, and $\alpha(0) = 0$. A function $\alpha : \mathbb{R}_{\geq 0} \to \mathbb{R}_{\geq 0}$ is of class $\mathcal{K}_\infty$ if it is a $\mathcal{K}$-function and $\alpha(s) \to +\infty$ as $s \to +\infty$.

Inspired by the work done in [31], this section derives a safety constraint for the optimal control input that guarantees the robot's spatial position, ξ_s, always lies within a defined safe set, $\mathcal{Z} \in \Re^3$. That is $\mathcal{Z}$ is forward invariant, i.e. if $\xi_s(0) = \xi_{s0} \in \mathcal{Z}$ then $\xi_s = \xi_s(t) \in \mathcal{Z}, \forall t$. The set $\mathcal{Z}$ is defined as:

$$\mathcal{Z} = \{\xi_s \in \mathbf{X} \subset \Re^3 | B(\xi_s) \geq 0\}, \tag{9a}$$

$$\partial\mathcal{Z} = \{\xi_s \in \mathbf{X} \subset \Re^3 | B(\xi_s) = 0\}, \tag{9b}$$

$$\mathrm{Int}(\mathcal{Z})\{\xi_s \in \mathbf{X} \subset \Re^3 | B(\xi_s) > 0\}. \tag{9c}$$

Let $\mathcal{Z}$ denote the superlevel set of a continuously differentiable function $B : \Re^3 \to \Re$. The function B qualifies as a CBF if there exists an $\mathcal{K}_\infty$-function γ for the control system (5) to satisfy:

$$\exists\ \mathcal{V}(t) \text{ s.t. } \dot{B}(\xi_s(t), \mathcal{V}(t)) \geq -\gamma B(\xi_s(t)), \gamma \in \mathcal{K}_\infty \tag{10}$$

Extending this inequality constraint to the discrete-time domain and using γ as a scalar, we can consider the set consisting of all control values at a point $\xi_s(k) \in \mathbf{X}$ as:

$$\begin{aligned}\kappa_{cbf} = \{\mathcal{V} \in \mathbf{U} : \Delta B(\xi_s(k), \mathcal{V}(k)) - \gamma B(\xi_s(k)) \geq 0,\\ 0 \leq \gamma \leq 1\}\end{aligned} \tag{11}$$

where $\Delta B(\xi_s(k), \mathcal{V}(k)) = B(\xi_s(k+1)) - B(\xi_s(k))$.

Remark 1. By Theorem 2 in [31], if B is a CBF in $\mathbf{X}$ and $\frac{\partial B}{\partial \xi_s}(\xi_s) \neq 0$ for all $\xi_s \in \partial\mathcal{Z}$, then any control signal $\mathcal{V} \in \kappa_{cbf}(\xi_s(k))$ for the system (5) renders the set $\mathcal{Z}$ safe. Additionally, the set $\mathcal{Z}$ is asymptotically stable in $\mathbf{X}$.

Most recent obstacle detection systems for AUVs using sonar and camera were reviewed in [35]. This paper focuses on control strategy design; hence, we assume that the AUV can detect obstacles through its sensors. The rigid body obstacle is conceptualized as a union of spheres with centroids $\varphi_{ob} = [x_{ob}, y_{ob}, z_{ob}]^T$ (m) and a fixed radius r_{ob} (m). Similarly, the AUV safety zone is defined by a sphere centred on the AUV with a radius r_{rb}. Safety sets for n obstacles are denoted as follows:

$$\mathcal{Z}_n = \{\xi_s(k) \in \mathbf{X} \subset \Re^3 : B_n(\xi_s(k), \mathcal{P}(k)) \geq 0\} \tag{12}$$

where

$$\begin{aligned}B_n(\xi_s(k), \mathcal{P}(k)) =& (x(k) - x_{ob,n}(k))^2 + (y(k) - y_{ob,n}(k))^2 \\ &+ (z(k) - z_{ob,n}(k))^2 - (r_{rb} + r_{ob,n})^2\end{aligned} \tag{13}$$

The parameter vector $\mathcal{P}$ is constructed to store obstacle information for the OCP discussed in the next section. To guarantee safe operation while regulating to the target state, the condition in (11) is incorporated into the OCP as a safety constraint. In our previous analysis on safety-critical control [33], the CBF with a relaxed decay rate of the barrier function simultaneously enhanced OCP feasibility, system safety, and computational efficiency compared to traditional CBF and Euclidean distance constraints. This study combines Relax-CBF with NMPC for AUV control problems.

C. NMPC-Relax-CBF for Trajectory Tracking Control

The subsequent section outlines the OCP setup for trajectory tracking of AUV1, which is configured to follow a predetermined path. The standard NMPC framework is developed by establishing and optimizing a cost function alongside constraints over the prediction horizon N. The OCP is detailed in a parametric format as described below:

$$\begin{aligned}J_{1N}(\xi_1(k), \mathcal{V}_1(k), \mathcal{P}_1(k)) = \min_{\mathbf{S}_1} \Bigg\{ &\Omega_1(\xi_1(k+N), \mathcal{P}_1(k)) \\ &+ \sum_{m=0}^{N-1} \Big(\Gamma_1(\varepsilon_1(m)) + \ell_1(\xi_1(k+m), \mathcal{V}_1(k+m), \mathcal{P}_1(k)) \Big) \Bigg\}\end{aligned} \tag{14a}$$

Subject to:

$$\xi_1(k) - \xi_{\text{fb},1} = 0, \tag{14b}$$

$$\xi_1(k+m+1) - \mathbf{F}_1(\xi_1(k+m), \mathcal{V}_1(k+m)) = 0, \tag{14c}$$

$$\xi_1(k+m) \in \mathbf{X},\ \mathcal{V}_1(k+m) \in \mathbf{U}, \tag{14d}$$

$$\begin{aligned}&B_n(\xi_{s1}(k+m+1), \mathcal{P}_1(k)) \\ &- \varepsilon_1(m)(1-\gamma) B_n(\xi_{s1}(k+m), \mathcal{P}_1(k)) \geq 0.\end{aligned} \tag{14e}$$

Where $\mathbf{S}_1$ contains decision variables as $\mathbf{S}_1 = [\xi_1(k)^T, ..., \xi_1(k+N)^T, \mathcal{V}_1(k)^T, ..., \mathcal{V}_1(k+N-1)^T, \varepsilon_1(k), ..., \varepsilon_1(k+N-1)]$. Besides obstacle information, parameter vector $\mathcal{P}$ also stores reference state vector ξ_r, desired velocity vector $\mathcal{V}_r$, and feedback state vector ξ_{fb}. Meanwhile, $\varepsilon_1(m)$ are decay-rate slack variables added to enhance the feasibility of the OCP, and the $\Gamma_1(\varepsilon_1(m))$ are included in the cost function to minimise those slack variables.

$$\Gamma_1(\varepsilon_1(m)) = w_{\varepsilon 1}(\varepsilon_1(m) - 1)^2 \tag{15}$$

where $w_{\varepsilon 1}$ is the positive penalty gains for the slack variables. The stage cost includes two quadratic terms: one will penalise the tracking error, and another will minimise the deviation of the control input from its reference value, $\ell_1 : \Re^6 \times \Re^6 \to \Re_{\geq 0}$. The terminal cost is a quadratic function of the state variable error, $\Omega_1 : \Re^6 \to \Re_{\geq 0}$.

$$\begin{aligned}\ell_1(\xi_1(k), \mathcal{V}_1(k), \mathcal{P}_1(k)) &= \xi_{e1}(k)^T W_{\xi 1} \xi_{e1}(k) \\ &\quad + (\mathcal{V}_1(k) - \mathcal{V}_{r1}(k))^T W_{u1} (\mathcal{V}_1(k) - \mathcal{V}_{r1}(k)), \\ \Omega_1(\xi_1(k), \mathcal{P}_1(k)) &= \xi_{e1}(k)^T W_{\Omega 1} \xi_{e1}(k).\end{aligned} \tag{16}$$

Where $W_{\xi 1}$, W_{u1}, and $W_{\Omega 1}$ are positive definite symmetric matrices.

The multiple shooting approach [36] is used to transform the OCP into a Nonlinear Program (NLP). Constructing a vector

that contains all decision variables as $\Xi_1 = \mathbf{S}_1^T$, the NLP is introduced as below:

$$\min_{\Xi_1} T_1(\Xi_1, \mathcal{P}_1) \ \ s.t. \begin{cases} H_1(\Xi_1, \mathcal{P}_1) = 0, \\ G_1(\Xi_1, \mathcal{P}_1) \leq 0. \end{cases} \tag{17}$$

The NLP constraints are categorized into two types: the equality constraint vector $H_1(\Xi_1, \mathcal{P}_1)$, which ensures compliance with the system dynamics as specified in (14b) and (14c), and the inequality constraint vector $G_1(\Xi_1, \mathcal{P}_1)$, which enforces the restrictions outlined in (14d) along with the safety constraints described in (14e), thereby keeping the decision variables within safe operational limits.

D. NMPC-Relax-CBF for Position Tracking Control

The follower's objective is to maintain a desired relative position with respect to its leader. All other agents $i = 2, ..., n$ are unaware of the desired path. Within a pair of AUVs, the leader broadcasts its state and formation vector to its follower at time step k. Thus, the following control framework for position tracking is suggested:

$$J_{iN}(\xi_i(k), \mathcal{V}_i(k), \mathcal{P}_i(k)) = \min_{\mathbf{S}_i} \Bigg\{ \Omega_i(\xi_i(k+N), \mathcal{P}_i(k)) + \sum_{m=0}^{N-1} \Big(\Gamma_i(\varepsilon_i(m)) + \ell_i(\xi_i(k+m), \mathcal{V}_i(k+m), \mathcal{P}_i(k)) \Big) \Bigg\} \tag{18a}$$

Subject to:

$$\xi_i(k) - \xi_{\text{fb},i} = 0, \tag{18b}$$

$$\xi_i(k+m+1) - \mathbf{F}_i(\xi_i(k+m), \mathcal{V}_i(k+m)) = 0, \tag{18c}$$

$$\xi_i(k+m) \in \mathbf{X}, \ \mathcal{V}_i(k+m) \in \mathbf{U}, \tag{18d}$$

$$B_n(\xi_{si}(k+m+1), \mathcal{P}_i(k)) - \varepsilon_i(m)(1-\gamma) B_n(\xi_{si}(k+m), \mathcal{P}_i(k)) \geq 0. \tag{18e}$$

$$\mathcal{D}_i(\xi_{sL}, \xi_{si}(k+m)) \leq \mathcal{C}. \tag{18f}$$

All constraints of OCP (18) are set up similarly to the OCP (14), only additional constraint (18f) guarantees the follower stays within the communication range with its leader. The stage cost, terminal cost, and distance constraint $\mathcal{D}_i$ are defined as:

$$\begin{aligned} &\ell_i(\xi_i(k), \mathcal{V}_i(k), \mathcal{P}_i(k)) = \\ &(\mathcal{V}_i(k) - \mathcal{V}_{ri}(k))^T W_{ui} (\mathcal{V}_i(k) - \mathcal{V}_{ri}(k)) + \\ &((\xi_L + \mathcal{A}_i) - \xi_i(k))^T W_{\xi i} ((\xi_L + \mathcal{A}_i) - \xi_i(k)), \\ &\Omega_i(\xi_i(k), \mathcal{P}_i(k)) = \\ &((\xi_L + \mathcal{A}_i) - \xi_i(k))^T W_{\Omega i} ((\xi_L + \mathcal{A}_i) - \xi_i(k)), \\ &\mathcal{D}_i(\xi_{sL}, \xi_{si}(k)) = \sqrt{(x_L - x_i)^2 + (y_L - y_i)^2 + (z_L - z_i)^2}. \end{aligned} \tag{19}$$

Where $W_{\xi i}$, W_{ui}, and $W_{\Omega i}$ are positive definite symmetric matrices.

Similar NLP for other agents in the team are constructed as

$$\min_{\Xi_i} T_i(\Xi_i, \mathcal{P}_i) \ \ s.t. \begin{cases} H_i(\Xi_i, \mathcal{P}_i) = 0, \\ G_i(\Xi_i, \mathcal{P}_i) \leq 0. \end{cases} \tag{20}$$

The proposed NMPC-Relax-CBF strategies are solved using an Interior Point OPTimizer (IPOPT). Based on the current feedback state and environmental data, the IPOPT solver derives an optimal trajectory $\boldsymbol{\xi}_N^*$, control sequence $\boldsymbol{\mathcal{V}}_{N-1}^*$, and slack variable $\boldsymbol{\varepsilon}_{N-1}^*$. The initial element of the optimized sequence $\boldsymbol{\mathcal{V}}_{N-1}^*$, designated as $\mathcal{V}_1^*(k)$, is subsequently implemented in the system. The remaining portion of the optimized sequence is utilized as the initial estimate for the decision variable vector in the following iteration. Consequently, the solver is re-engaged to determine new control input values. This control strategy is outlined in Algorithm 1.

Algorithm 1 IPOPT - NMPC-Relax-CBF

Given Ξ_i^0
Initialise $(m, \Xi_i^m) \leftarrow (0, \Xi_i^0)$
while ControllerIsRunning() **do**
  $\xi_{\text{fb},i} \leftarrow$ StateFeedback()
  ξ_r / ξ_L, $\mathcal{A}_i \leftarrow$ Commands()
  $\varphi_{ob,n} \leftarrow$ Sensors
  $\mathcal{P}_i \leftarrow [\xi_{\text{fb},i}^T, \xi_r^T / \xi_L^T, \mathcal{A}_i^T, \varphi_{ob,n}^T]^T$
  $\Xi_i^{m+1} \leftarrow$ IPOPT solver$(\Xi_i^m, \mathcal{P}_i)$
  $\boldsymbol{\mathcal{V}}_{N-1,i}^* \leftarrow$ ExtractInputSequence(Ξ_i^{m+1})
  $\mathcal{V}_{1,i}^*(k) \leftarrow$ ExtractFirstInput$(\boldsymbol{\mathcal{V}}_{N-1,i}^*)$
  AUV$_i \leftarrow$ ApplyInput$(\mathcal{V}_{1,i}^*(k))$
  $\Xi_i^{m+2} \leftarrow$ Shift$(\boldsymbol{\xi}_{N,i}^*, \boldsymbol{\mathcal{V}}_{N-1,i}^*, \boldsymbol{\varepsilon}_{N-1,i}^*)$
  $m \leftarrow m + 1$
end while

E. Stability Analysis

Consider that system (5) is controlled by the NMPC control law $\kappa(k) = \mathcal{V}_1^*(k)$, obtained from NLP (17) or NLP (20), then a closed loop system can be expressed as:

$$\xi(k+1) = \mathbf{F}(\xi(k), \kappa(k)) \tag{21}$$

Definition 2. $\mathbf{X}_f$ is a forward invariant set for the system (5), i.e. for all $\xi(k) \in \mathbf{X}_f$ there exists $\kappa(k)$ such that $\mathbf{F}(\xi(k), \kappa(k)) \in \mathbf{X}_f$. A continuous function Ω is a Control Lyapunov Function (CLF) in $\mathbf{X}_f$ for all $\xi(k) \in \mathbf{X}_f$ if the following holds:

1) There exist $\mathcal{K}_\infty$-function α_1 and α_2 satisfying

$$\alpha_1(\|\xi_e(k)\|) \leq \Omega(\xi(k), \mathcal{P}(k)) \leq \alpha_2(\|\xi_e(k)\|) \tag{22}$$

2) The decay rate of Ω is bounded by a positive function

$$\begin{aligned} &\Omega(\mathbf{F}(\xi(k), \kappa(k)), \mathcal{P}(k)) - \Omega(\xi(k), \mathcal{P}(k)) \\ &+ (\ell(\xi(k), \kappa(k), \mathcal{P}(k)) + \Gamma(\varepsilon(k))) \leq 0 \end{aligned} \tag{23}$$

Assumption 1. There exists a control input $\kappa(k) \in \mathbf{U}$ for all $\xi, \xi_r \in \mathbf{X}$ that satisfy $\|\xi(k+1) - \xi_r\|^2 < \|\xi(k) - \xi_r\|^2$.

Remark 2. This assumption refers to the controllability properties of the AUV, where the AUV's thrusters are functioning correctly and within their designed operational parameters. The fulfilment of the accessibility rank condition guarantees that every point in the state space can be reached. Thus, there exists a path from the current configuration $\xi(k)$ to a new configuration $\xi(k+1)$ that aligns with the reference state ξ_r. The steady decrease of the cost function $J_{iN}(\cdot)$ in (14) and (18) and the systematic convergence of the system's state variables towards the desired configuration

in control Algorithm 1 will be established in Theorem 2. First, we present Theorem 1, which provides the necessary groundwork.

Theorem 1. Let Assumption 1 hold, then the terminal cost function Ω is a CLF on $D \in \mathbb{R}^6$, where D is a small neighborhood of the reference state.

Proof. Considering the diagonal matrices, $W_\xi = \text{diag}(w_\xi, w_\xi, w_\xi, w_\xi, w_\xi, w_\xi)$, $W_u = \text{diag}(w_u, w_u, w_u, w_u, w_u, w_u)$, and $W_\Omega = \text{diag}(w_\Omega, w_\Omega, w_\Omega, w_\Omega, w_\Omega, w_\Omega,)$, where w_ξ, w_u, w_Ω are strictly positive constants, the stage cost and terminal cost are rewritten as:

$$\begin{aligned}\ell(\xi(k), \kappa(k), \mathcal{P}(k)) &= w_\xi \|\xi(k) - \xi_r(k)\|^2 \\ &\quad + w_u \|\mathcal{V}(k) - \mathcal{V}_r(k)\|^2, \\ \Omega(\xi(k), \mathcal{P}(k)) &= w_\Omega \|\xi(k) - \xi_r(k)\|^2.\end{aligned} \tag{24}$$

Substituting (24) into (23) yields:

$$\begin{aligned}&w_\Omega \|\xi(k+1) - \xi_r(k)\|^2 - w_\Omega \|\xi(k) - \xi_r(k)\|^2 + w_\varepsilon(\varepsilon - 1)^2 \\ &+ w_\xi \|\xi(k) - \xi_r(k)\|^2 + w_u \|\mathcal{V}(k) - \mathcal{V}_r(k)\|^2 \leq 0\end{aligned} \tag{25}$$

Under the Assumption 1, it can be proven that:

$$\begin{aligned}&w_\Omega \Lambda + w_\xi \|\xi(k) - \xi_r(k)\|^2 + w_u \|\mathcal{V}(k) - \mathcal{V}_r(k)\|^2 \\ &+ w_\varepsilon(\varepsilon - 1)^2 \\ &\leq w_\Omega \Lambda + w_\xi \|\xi_e(k)\|^2 + w_u \|\mathcal{V}_{max} - \mathcal{V}_r(k)\|^2 + w_\varepsilon \leq 0\end{aligned} \tag{26}$$

where $\Lambda = \|\xi(k+1) - \xi_r(k)\|^2 - \|\xi(k) - \xi_r(k)\|^2$. By choosing $w_\Omega \geq \frac{w_\xi \|\xi_e(k)\|^2 + w_u \|\mathcal{V}_{max} - \mathcal{V}_r(k)\|^2 + w_\varepsilon}{|\Lambda|}$ the inequality (23) is satisfied and the terminal cost $\Omega(\cdot)$ is a CLF.

Remark 3. Within a small proximity of the reference state, as $\Lambda \to 0$ ($\xi \to \xi_r$), the inequality in (26) is not satisfied. Hence, selecting a higher value for w_Ω ensures that this vicinity remains close to ξ_r. Parameters w_ξ, w_u, w_Ω can be fine-tuned using a trial and error approach to achieve satisfactory performance.

Assumption 2. There exists a $\mathcal{K}_\infty$-function α_3 such that the state cost satisfies $\ell(\xi(k), \kappa(k), p(k)) \geq \alpha_3(\|\xi_e(k)\|)$ for all $\xi \in \mathbf{X}$ and $\mathcal{V} \in \mathbf{U}$. This is a common assumption in the design of NMPC [37], [38].

Theorem 2. Assume that W_Ω is selected based on Theorem 1 and Assumptions 1 and 2 are satisfied, then the closed-loop system (21) is asymptotically stable in a neighbourhood of the desired state $D : \|\xi_e\| < \zeta$.

Proof. Considering the optimal value function $J_N^*(\xi^*(k), \kappa(k), \mathcal{P}(k))$ as a Lyapunov function candidate, recall the cost function in (14) or (18)

$$\begin{aligned}J_N(\xi(k), \mathcal{V}(k), \mathcal{P}(k)) &= \Omega(\xi(k+N), \mathcal{P}(k)) \\ &+ \sum_{m=0}^{N-1} \Big(\Gamma(\varepsilon(m)) + \ell(\xi(k+m), \mathcal{V}(k+m), \mathcal{P}(k)) \Big) \\ &= \sum_{m=0}^{N-2} \Big(\Gamma(\varepsilon(m)) + \ell(\xi(k+m), \mathcal{V}(k+m), \mathcal{P}(k)) \Big) \\ &+ \Omega(\xi(k+N), \mathcal{P}(k)) \\ &+ \Gamma(\varepsilon(N-1)) + \ell(\xi(k+N-1), \mathcal{V}(k+N-1), \mathcal{P}(k))\end{aligned} \tag{27}$$

Taking into account the cost function for $(N-1)$ prediction horizon as follows:

$$\begin{aligned}J_{N-1}(\xi(k), \mathcal{V}(k), \mathcal{P}(k)) &= \Omega(\xi(k+N-1), \mathcal{P}(k)) \\ &+ \sum_{m=0}^{N-2} \Big(\Gamma(\varepsilon(m)) + \ell(\xi(k+m), \mathcal{V}(k+m), \mathcal{P}(k)) \Big)\end{aligned} \tag{28}$$

Substituting (28) into (27) yields:

$$\begin{aligned}&J_N(\xi(k), \mathcal{V}(k), \mathcal{P}(k)) - J_{N-1}(\xi(k), \mathcal{V}(k), \mathcal{P}(k)) = \\ &\quad \Omega(\xi(k+N), \mathcal{P}(k)) - \Omega(\xi(k+N-1), \mathcal{P}(k)) \\ &\quad + \Gamma(\varepsilon(N-1)) + \ell(\xi(k+N-1), \mathcal{V}(k+N-1), \mathcal{P}(k))\end{aligned} \tag{29}$$

From Theorem 1, it is inferred that

$$J_N(\xi(k), \mathcal{V}(k), \mathcal{P}(k)) < J_{N-1}(\xi(k), \mathcal{V}(k), \mathcal{P}(k)) \tag{30}$$

This inequality extends to the corresponding optimal value functions:

$$\begin{aligned}&J_N^*(\xi^*(k), \kappa(k), \mathcal{P}(k)) = \inf_{\mathcal{V}(\cdot) \in \mathbf{U}} J_N(\xi(k), \mathcal{V}(k), \mathcal{P}(k)) \\ &\leq \inf_{\mathcal{V}(\cdot) \in \mathbf{U}} J_{N-1}(\xi(k), \mathcal{V}(k), \mathcal{P}(k)) = J_{N-1}^*(\xi^*(k), \kappa(k), \mathcal{P}(k))\end{aligned} \tag{31}$$

Bellman's principle of optimality [39] is used to obtain the relationship of optimal value functions at different horizons N and points in space. This approach yields

$$\begin{aligned}J_N^*(\xi^*(k), \kappa(k), \mathcal{P}(k)) &= \ell(\xi^*(k), \kappa(k), \mathcal{P}(k)) + \Gamma(\varepsilon^*(k)) \\ &+ J_{N-1}^*(\xi^*(k+1), \kappa(k+1), \mathcal{P}(k+1))\end{aligned} \tag{32}$$

From Assumption 2, the lower bound of the optimal value function is defined as:

$$\begin{aligned}J_N^*(\xi^*(k), \kappa(k), \mathcal{P}(k)) &\geq \ell(\xi^*(k), \kappa(k), \mathcal{P}(k)) \\ &\geq \alpha_3(\|\xi^*(k) - \xi_r(k)\|)\end{aligned} \tag{33}$$

Expanding (31) consecutively from N to 1 leads to:

$$\begin{aligned}&J_N^*(\xi^*(k), \kappa(k), \mathcal{P}(k)) \leq J_{N-1}^*(\xi^*(k), \kappa(k), \mathcal{P}(k)) \\ &\leq \cdots \leq J_1^*(\xi^*(k), \kappa(k), \mathcal{P}(k)) \leq \Omega(\xi^*(k+1), \mathcal{P}(k)) \\ &\leq \alpha_2(\|\xi^*(k+1) - \xi_r(k)\|)\end{aligned} \tag{34}$$

Considering the difference between the J_N^* evaluated at k and $k+1$, using the Bellman equation in (32), and the inequality in (31)

$$\begin{aligned}&J_N^*(\xi^*(k+1), \kappa(k+1), \mathcal{P}(k+1)) - J_N^*(\xi^*(k), \kappa(k), \mathcal{P}(k)) \\ &= J_N^*(\xi^*(k+1), \kappa(k+1), \mathcal{P}(k+1)) - \ell(\xi^*(k), \kappa(k), \mathcal{P}(k)) \\ &- \Gamma(\varepsilon^*(k)) - J_{N-1}^*(\xi^*(k+1), \kappa(k+1), \mathcal{P}(k+1)) \\ &\leq -(\ell(\xi^*(k), \kappa(k), \mathcal{P}(k)) + \Gamma(\varepsilon^*(k)))\end{aligned} \tag{35}$$

By Definition 2, $J_N^*(\xi^*(k), \kappa(k), \mathcal{P}(k))$ is a control Lyapunov function, and the closed-loop system (21) is asymptotically stable to the desired state.

Remark 4. It should be noted that the terminal cost function $\Omega(\cdot)$ may not qualify as a CLF as the robot's state approaches the vicinity D where $\|\xi_e\| < \zeta$. Consequently, the aforementioned property does not hold in this domain. However, the initial values of the control sequence in Ξ can be set to zero for all $\xi(k) \in D$. The resulting OCP for the next step becomes $J_N(\xi(k+1), \mathcal{V}(k), \mathcal{P}(k)) \leq (N-1)w_\xi \zeta + w_\Omega \zeta$, which serves

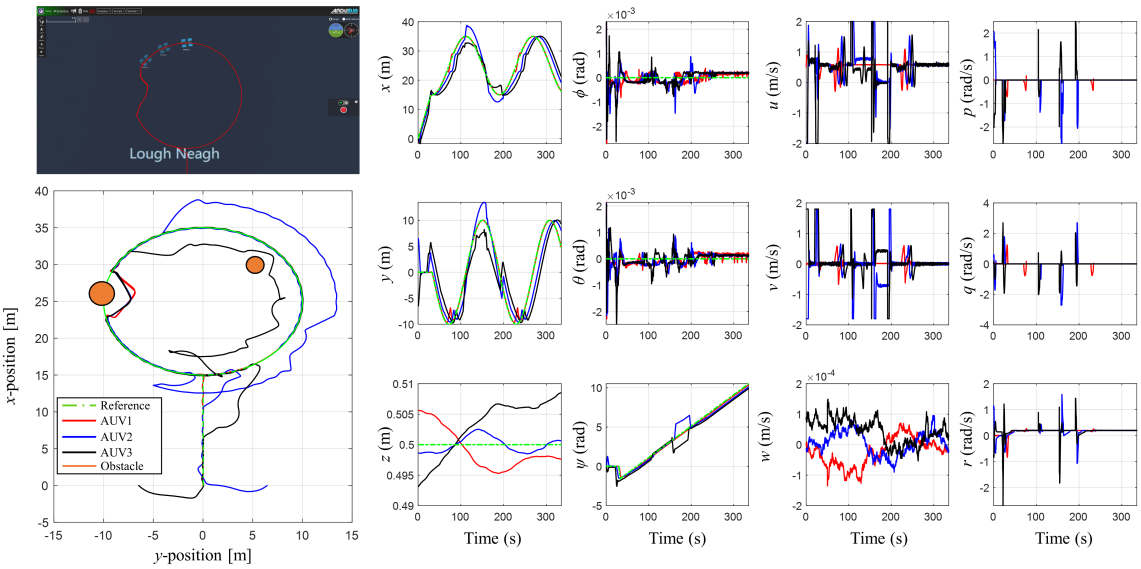

Fig. 3. Circle trajectory tracking and formation control in SITL simulation.

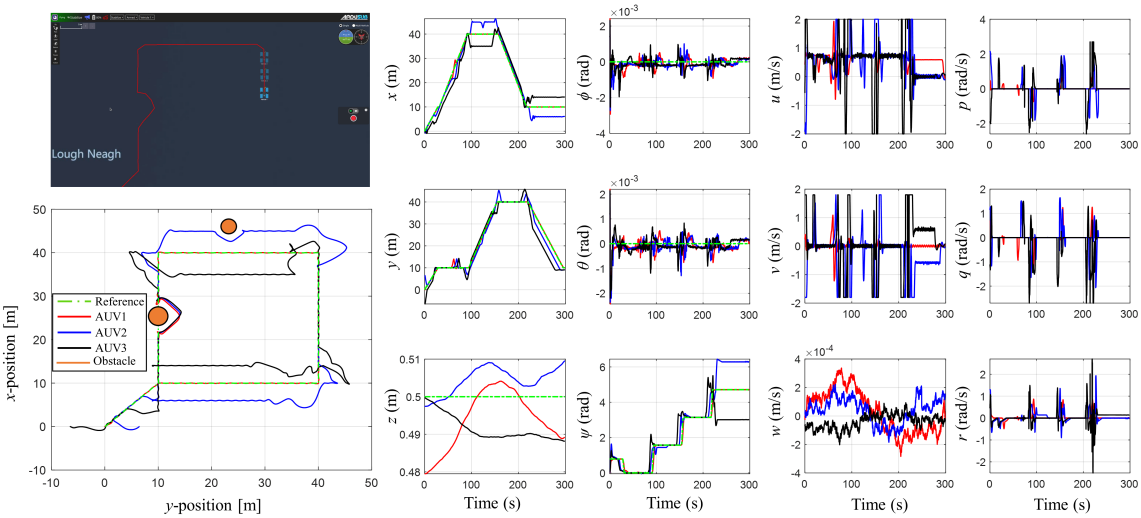

Fig. 4. Square trajectory tracking and formation control in SITL simulation.

as an upper bound for $J_N^*(\xi^*(k+1), \kappa(k), \mathcal{P}(k))$. Therefore, selecting a sufficiently large w_Ω ensures that the system's trajectory remains confined within the region D.

Remark 5. As proven by Theorem 3.5 in [39], the proposed scheme for the closed-loop system (21) is recursively feasible. Furthermore, with the implementation of the relaxed decay-rate technique for the barrier function, as analyzed in [34] and [33], the safety performance of agents is enhanced by allowing a slower decrease in the barrier function while not harming the feasibility of the OCP.

IV. Results and Discussion

A. ArduPilot Software-In-The-Loop Simulation

To test the NMPC-Relax-CBF code intended for the BlueRov2, we utilized the ArduPilot SITL open-source package. This simulation operated in real-time with an independently generated model of the BlueRov2, using the same software control interfaces as the AUV hardware. Three AUVs followed a circle with a diameter of 20 m, as shown in Fig. 3, and a 20x20 m square, as shown in Fig. 4, with random static obstacles along the paths. Three different formations were configured during the tracking, as shown in Table I. The sampling time for all agents was chosen as $\tau_i = 0.1$ s and the prediction horizon $N_i = 30$. The CBF parameter was chosen based on the observed robot performance, with a smaller value of γ enhancing safety performance. Therefore, $\gamma_i = 0.1$ was chosen for all AUVs, effectively generating smooth trajectories and improving the robots' ability to avoid obstacles. The penalty gain for the slack variables w_ε regulated the proximity of ε to 1 to minimise the deviation from the nominal decay rate, and it was not set too small to avoid over-relaxing the CBF constraints. Hence, $w_{\varepsilon,i} = 10$ was chosen for all agents. The try-and-error method was used to tune the controller's weights. For the trajectory tracking of AUV1, the weights for the state and control inputs were chosen as

TABLE I
FORMATION CONTROL REFERENCE - SITL SIMULATION

Time	$\mathcal{A}_1$	$\mathcal{A}_2$	Case study
0-30 s	$[-4\cos(\psi_1), -4\sin(\psi_1), 0, 0, 0, 0]^T$	$[-4\cos(\psi_2), -4\sin(\psi_2), 0, 0, 0, 0]^T$	1
30-109 s	$[-4\cos(\psi_1 - 0.25), -4\sin(\psi_1 - 0.25), 0, 0, 0, 0]^T$	$[-4\cos(\psi_2 - 0.25), -4\sin(\psi_2 - 0.25), 0, 0, 0, 0]^T$	
109-155 s	$[-3\cos(\psi_1) + 3\sin(\psi_1), -3\sin(\psi_1) - 3\cos(\psi_1), 0, 0, 0, 0]^T$	$[-6\sin(\psi_2), 6\cos(\psi_2), 0, 0, 0, 0]^T$	
155-190 s	$[\cos(\psi_1) + 2.5\sin(\psi_1), \sin(\psi_1) - 2.5\cos(\psi_1), 0, 0, 0, \pi/2]^T$	$[-5\cos(\psi_2), -5\sin(\psi_2), 0, 0, 0, -\pi]^T$	
190-335 s	$[-4\cos(\psi_1 - 0.25), -4\sin(\psi_1 - 0.25), 0, 0, 0, 0]^T$	$[-4\cos(\psi_2 - 0.25), -4\sin(\psi_2 - 0.25), 0, 0, 0, 0]^T$	
0-97 s	$[-4\cos(\psi_1), -4\sin(\psi_1), 0, 0, 0, 0]^T$	$[-4\cos(\psi_2), -4\sin(\psi_2), 0, 0, 0, 0]^T$	2
97-153 s	$[-3\cos(\psi_1) + 3\sin(\psi_1), -3\sin(\psi_1) - 3\cos(\psi_1), 0, 0, 0, 0]^T$	$[-6\sin(\psi_2), 6\cos(\psi_2), 0, 0, 0, 0]^T$	
153-224 s	$[-4\cos(\psi_1), -4\sin(\psi_1), 0, 0, 0, 0]^T$	$[-4\cos(\psi_2), -4\sin(\psi_2), 0, 0, 0, 0]^T$	
224-299 s	$[\cos(\psi_1) + 2.5\sin(\psi_1), \sin(\psi_1) - 2.5\cos(\psi_1), 0, 0, 0, \pi/2]^T$	$[-5\cos(\psi_2), -5\sin(\psi_2), 0, 0, 0, -\pi]^T$	

$W_{\xi,1} = \text{diag}(7, 7, 3, 1, 1, 10)$, $W_{u,1} = \text{diag}(3, 3, 1, 1, 1, 3)$, and $W_{\Omega,1} = 10^3 * \text{diag}(1, 1, 1, 1, 1, 1)$. For the point stabilization of AUV2 and AUV3, $W_{\xi,i} = \text{diag}(30, 30, 5, 1, 1, 30)$, $W_{u,i} = \text{diag}(5, 5, 1, 1, 1, 10)$, and $W_{\Omega,i} = 10^3 * \text{diag}(1, 1, 1, 1, 1, 1)$ for $i = 2, 3$. The state weights were increased to achieve a faster response in the formation adjustment. The simulation results demonstrated that both trajectory tracking and formation control were successfully achieved, with safety ensured by the Relax-CBF.

B. Real-time Experiment

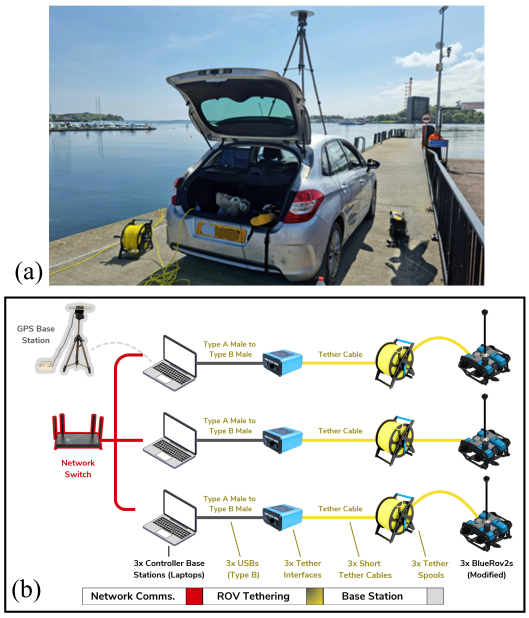

Fig. 5. (a) Experimental hardware setup. (b) Communication diagram

1) Experimental Setup: This section detailed the outdoor experimental setup used to verify the proposed approach on three BlueRov2 (heavy configuration) underwater robots, as shown in Fig 5 (a). The test locations were Queen's University Belfast (QUB) Marine Laboratory in Portaferry and QUB Boat Club in Lagan. The main challenges at these locations were seaweed, tides, and river currents. Fig 5 (b) shows the communication diagram for the multi-AUVs system. We accessed the onboard Auto-Pilot (AP) via tether using the Mavlink protocol. Mavlink handled data between the topside computer and AUV, while ROS communications occurred over a local gigabit Ethernet with one AUV control computer as the ROS-Master node.

Orientation angles were reasonably well estimated by low-cost sensors, gyro, and accelerometer. However, a major challenge for trajectory tracking controllers in underwater systems was accurately measuring current position states. To address this, we added a GPS/GNSS sensor on an elevated mast to each AUV system, allowing independent localization within the working area. We used the ArduSimple-RTK2B-GPS-RTK-Receiver-Kit with the modern u-blox F9P GPS processing module, which came with a compact active multi-band (L1/L2/E5b) antenna and RTK capability for more accurate positioning. To improve the accuracy of the localisation, a fixed base station with a clear sky view was added nearby. Fig 5 (b) also shows the hardware upgrade on the BlueRov2. The antenna was mounted to the main frame using a plastic top plate designed to bolt to existing fixing holes on the outer frame.

To obtain the same NED frame for the three AUVs, we set the same root GPS (lat, lon, alt) location for the three units, then used the Pymap3d function 'geodetic2ned' to convert individual feedback GPS signals to corresponding positions in a common NED frame. Our hardware modifications required the GPS antenna to remain above the water's surface. We ignored vertical ("down") offsets and adjusted the offsets for follower AUVs' local frames to ensure all AUVs used a common frame for relative positioning.

2) Line Tracking and Formation Control of Multiple BlueRov2 at The Open Sea: The following section demonstrated the effectiveness of the NMPC-Relaxed-CBF control strategy in guiding multiple BlueRov2 vehicles along a predefined trajectory with different desired formations in an open sea environment. AUV1 was controlled to follow a line from $\xi_{r1} = [5.7, -8, 0.5, 0, 0, -2.7]^T$ to $\xi_{r2} = [6.7, -33, 0.5, 0, 0, -2.7]^T$ with a fixed velocity of 0.4 m/s, and other AUVs tracked the desired positions to maintain formations as shown in Fig 6. The AUVs transitioned between three different formations during the mission. These transitions were presented in Table II. A virtual obstacle was located at $\varphi_{ob} = [5, -25, 0.5]^T$ (m) with a radius $r_{ob} = 1.5$ m, which was indicated by the brown circle. The hyperparameters $\tau_i = 0.1$ s, $N_i = 40$, $\gamma_i = 0.1$, $w_{\varepsilon,i} = 10$ were chosen for all agents. For the trajectory

TABLE II
FORMATION CONTROL REFERENCE - REAL-TIME EXPERIMENT

Time	$\mathcal{A}_1$	$\mathcal{A}_2$	Case study
0-15 s	$[-2\cos(\psi_1)+2\sin(\psi_1), -2\sin(\psi_1)-2\cos(\psi_1), 0, 0, 0, 0]^T$	$[-4\sin(\psi_2), 4\cos(\psi_2), 0, 0, 0, 0]^T$	1
15-63 s	$[-2\cos(\psi_1), -2\sin(\psi_1), 0, 0, 0, 0]^T$	$[-\cos(\psi_2), -\sin(\psi_2), 0, 0, 0, 0]^T$	
63-85 s	$[3\sin(\psi_1), -3\cos(\psi_1), 0, 0, 0, \pi/2]^T$	$[6\cos(\psi_2), -6\sin(\psi_2), 0, 0, 0, -\pi]^T$	
0-47 s	$[-5\cos(\psi_1), -5\sin(\psi_1), 0, 0, 0, 0]^T$	$[3\cos(\psi_2), 3\sin(\psi_2), 0, 0, 0, \pi/2]^T$	2
47-93 s	$[-2\cos(\psi_1), -2\sin(\psi_1), 0, 0, 0, 0]^T$	$[-\cos(\psi_2), -\sin(\psi_2), 0, 0, 0, 0]^T$	
93-109 s	$[-5\cos(\psi_1), -5\sin(\psi_1), 0, 0, 0, 0]^T$	$[3\cos(\psi_2), 3\sin(\psi_2), 0, 0, 0, \pi/2]^T$	
0-73.5 s	$[-5\cos(\psi_1), -5\sin(\psi_1), 0, 0, 0, 0]^T$	$[3\cos(\psi_2), 3\sin(\psi_2), 0, 0, 0, \pi/2]^T$	3
73.5-95 s	$[-2\cos(\psi_1), -2\sin(\psi_1), 0, 0, 0, 0]^T$	$[-\cos(\psi_2), -\sin(\psi_2), 0, 0, 0, 0]^T$	
0-15 s	$[-\cos(\psi_1)+2\sin(\psi_1), -\sin(\psi_1)-2\cos(\psi_1), 0, 0, 0, 0]^T$	$[-4\sin(\psi_2), 4\cos(\psi_2), 0, 0, 0, 0]^T$	4
15-25 s	$[\cos(\psi_1)+2\sin(\psi_1), \sin(\psi_1)-2\cos(\psi_1), 0, 0, 0, 0]^T$	$[-4\sin(\psi_2), 4\cos(\psi_2), 0, 0, 0, 0]^T$	
25-36 s	$[2\cos(\psi_1)+3\sin(\psi_1), 2\sin(\psi_1)-3\cos(\psi_1), 0, 0, 0, 0]^T$	$[-6\sin(\psi_2), 6\cos(\psi_2), 0, 0, 0, \pi/2]^T$	
36-73 s	$[-\cos(\psi_1)+2\sin(\psi_1), -\sin(\psi_1)-2\cos(\psi_1), 0, 0, 0, 0]^T$	$[-4\sin(\psi_2), 4\cos(\psi_2), 0, 0, 0, 0]^T$	
73-97 s	$[\cos(\psi_1)+2\sin(\psi_1), \sin(\psi_1)-2\cos(\psi_1), 0, 0, 0, 0]^T$	$[-4\sin(\psi_2), 4\cos(\psi_2), 0, 0, 0, 0]^T$	

tracking of AUV1, the weights for the state and control inputs were chosen as $W_{\xi,1} = \text{diag}(10, 10, 5, 1, 1, 100)$, $W_{u,1} = \text{diag}(5, 5, 1, 1, 1, 50)$, and $W_{\Omega,1} = 10^4 * \text{diag}(1, 1, 1, 1, 1, 1)$. High gains were selected for the yaw angle to compensate for the disturbance caused by the tether cable. For the point stabilization of AUV2 and AUV3, $W_{\xi,i} = \text{diag}(30, 30, 5, 1, 1, 100)$, $W_{u,i} = \text{diag}(5, 5, 1, 1, 1, 50)$, and $W_{\Omega,i} = 10^4 * \text{diag}(1, 1, 1, 1, 1, 1)$ for $i = 2, 3$. The state

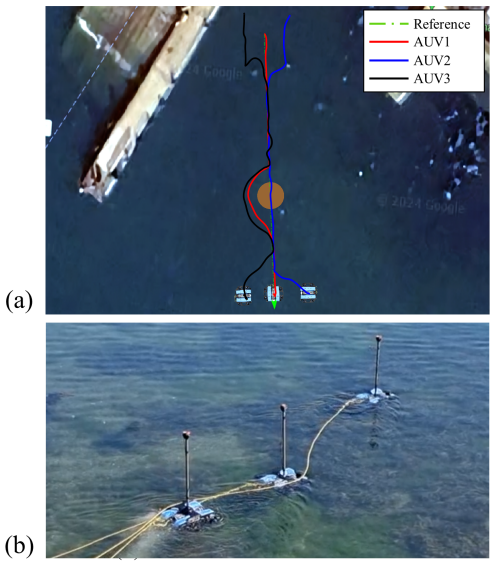

Fig. 6. (a) Overhead view of AUV trajectories. (b) Ground-level view of AUVs in Portaferry.

tracking performance of three AUVs was plotted in Fig 7 with the initial poses as $\xi_{0,1} = [5.8, -7.5, 0.53, 0, 0, -2.65]^T$, $\xi_{0,2} = [8.2, -6, 0.47, 0, 0, -2.82]^T$, and $\xi_{0,3} = [3.8, -5.9, 0.55, 0, 0, -3.1]^T$ and $\mathcal{V}_i = 0_{6\times1}, i \in \{1, 2, 3\}$ were the initial velocities. The x, y, and z position plots showed that AUV1 exhibited effective trajectory tracking. Transitions between formations were executed with minor deviations but were generally well-maintained. Furthermore, the proposed strategies successfully navigated AUV1 and AUV3 along the desired path without compromising safety. Each agent had its own Relax-CBF, allowing them to detect and avoid obstacles independently. Moreover, to eliminate the effect of obstacle avoidance manoeuvres on the follower trajectory, the leader broadcasted its reference pose instead of its current pose when encountering an obstacle. Notably, AUV2 drove through the virtual obstacle. This behaviour occurred because the Relax-CBF of AUV2 was intentionally disabled to provide crucial data for assessing the system's performance. This decision was made to simplify the process of locating the virtual obstacle, particularly since the robot was operating at a significant distance from the base computer. The optimal control signals for velocities and the Pulse Width

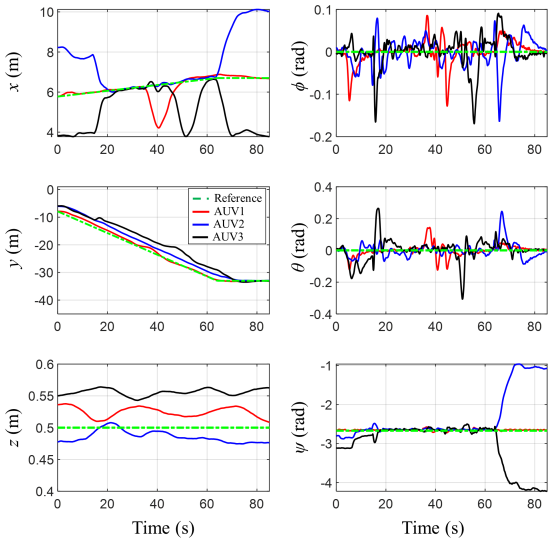

Fig. 7. Position and orientation tracking of AUV1, AUV2, and AUV3

Modulation (PWM) control inputs for the thrusters of the three AUVs were plotted in Fig 8 and Fig 9. The velocity plots demonstrated that AUV1 maintained relatively stable forward motion, while AUV2 and AUV3 exhibited more significant variations, particularly in the lateral direction and yaw angle, reflecting their dynamic roles in formation maintenance. The thruster's PWM revealed that AUV1 had stable control efforts with occasional spikes, whereas AUV2 displayed less variability around the obstacle due to its disabled Relax-CBF.

AUV3 exhibited the highest variability, indicating a reactive control strategy to handle the dynamic formation changes and interactions with the obstacle. Overall, the proposed schemes effectively and safely handled the complexities of multi-AUV coordination and formation maintenance in an open sea environment.

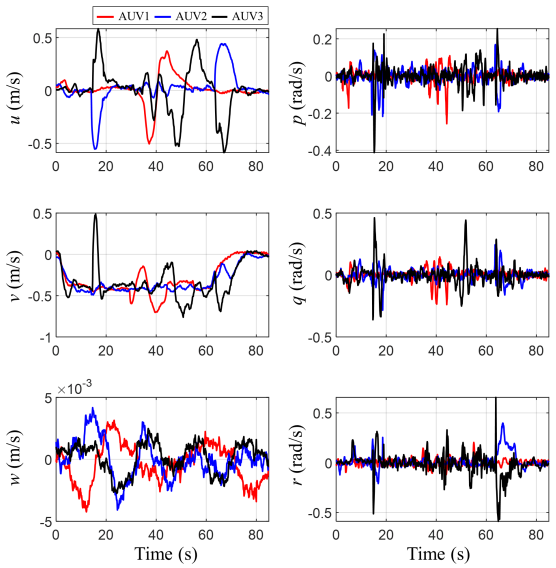

Fig. 8. Optimal control signals of AUV1, AUV2, and AUV3

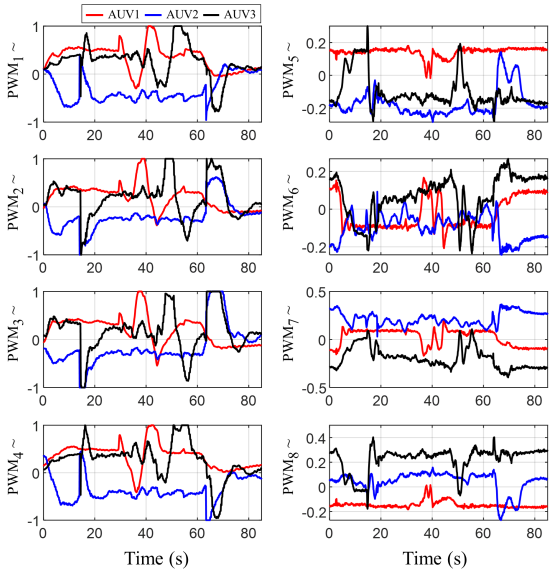

Fig. 9. Normalised PWM for eight thrusters of AUV1, AUV2, and AUV3

3) Square Tracking and Formation Control of Multiple BlueRov2 at The River: This section presented the square tracking and formation control performance of the NMPC-Relaxed-CBF for multiple BlueRov2 vehicles in a river environment. AUV1 was controlled to form a square from an initial corner at $\xi_{r1} = [5, 17, 0.5, 0, 0, 6.2]^T$ with an edge length of 10 m and a fixed velocity of 0.3 m/s, and other AUVs tracked the desired positions to maintain formations as shown in Fig 10. The AUVs transitioned between three formations during the mission. These transitions were presented in Table II. All of the controller parameters were selected to be the same as in Section B-2.

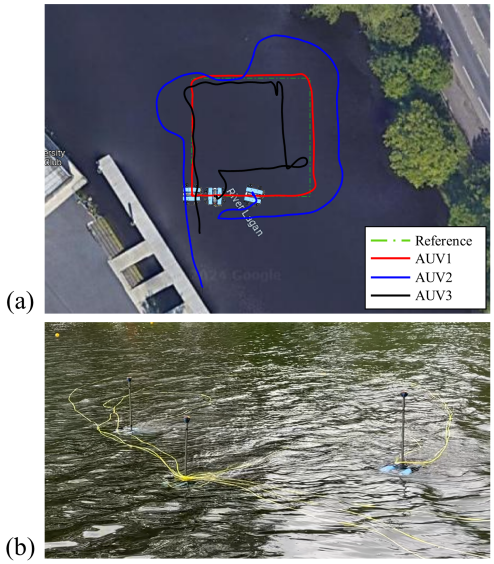

Fig. 10. (a) Overhead view of AUV trajectories. (b) Ground-level view of AUVs in Lagan.

The state tracking performance of three AUVs was plotted in Fig 11 with the initial poses as $\xi_{0,1} = [4.7, 17.5, 0.47, 0, 0, 5.8]^T$, $\xi_{0,2} = [5.7, 9.3, 0.48, 0, 0, 5.47]^T$, and $\xi_{0,3} = [5.5, 14, 0.51, 0, 0, 2.8]^T$ and $\mathcal{V}_i = 0_{6\times1}, i \in \{1, 2, 3\}$ were the initial velocities. AUV1 closely followed the reference x and y positions with minor deviations, while AUV2 and AUV3 exhibited more significant variations, particularly during transition periods around 40 to 60 s, indicating the challenges of maintaining formation during sharp turns and under the influence of river flow disturbances. The z position plot showed that all AUVs maintained relatively stable depths. The ϕ_i and θ_i angles exhibited small fluctuations, with more pronounced variations during transitions, highlighting the dynamic adjustments required for stability. AUV3 displayed larger variations in ψ_3 due to a 90-degree offset in formation. As observed, the NMPC-Relaxed-CBF control strategy still effectively managed the square tracking and formation control of the AUVs in response to the river current, with AUV2's higher variability underscoring its role in dynamically adjusting to maintain formation. The optimal control signals for velocities and the PWM control inputs of the three AUVs were plotted in Fig 12 and Fig 13. The velocity plots showed that AUV1 maintained relatively stable forward and lateral velocities, while AUV2 and AUV3 exhibited more significant variations, especially during formation changes. This indicated the dynamic adjustments needed for formation maintenance. Consequently, the PWM control inputs for AUV1 showed stable control efforts with occasional spikes, while AUV2 and AUV3 displayed more variability.

4) Circle Tracking and Formation Control of Multiple BlueRov2 at The River: Similar to Section C, the NMPC-Relaxed-CBF control strategy was verified by a persistent excitation trajectory in the river environment. The reference

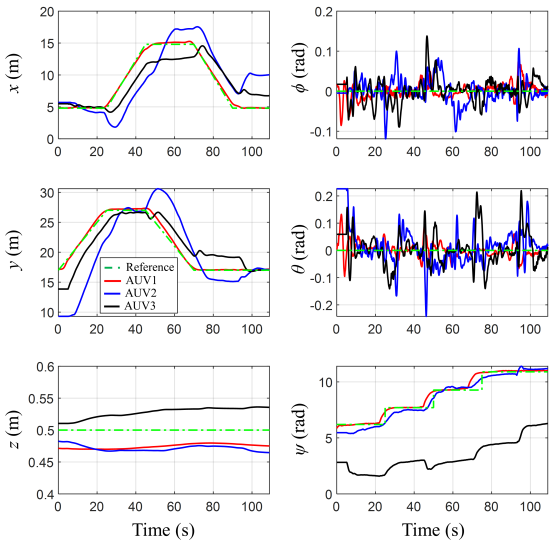

Fig. 11. Position and orientation tracking of AUV1, AUV2, and AUV3

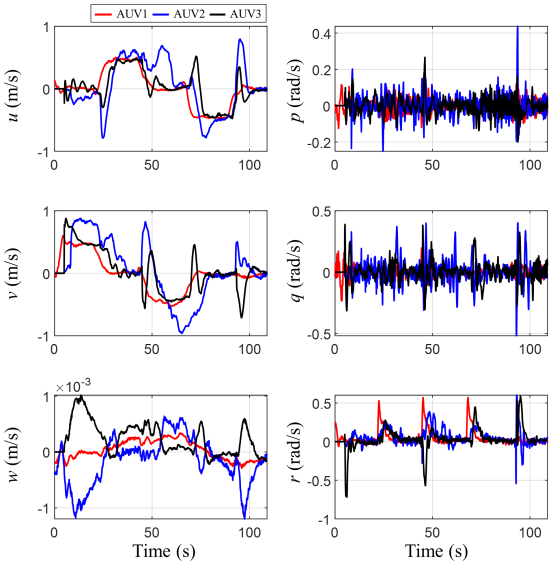

Fig. 12. Optimal control signals of AUV1, AUV2, and AUV3

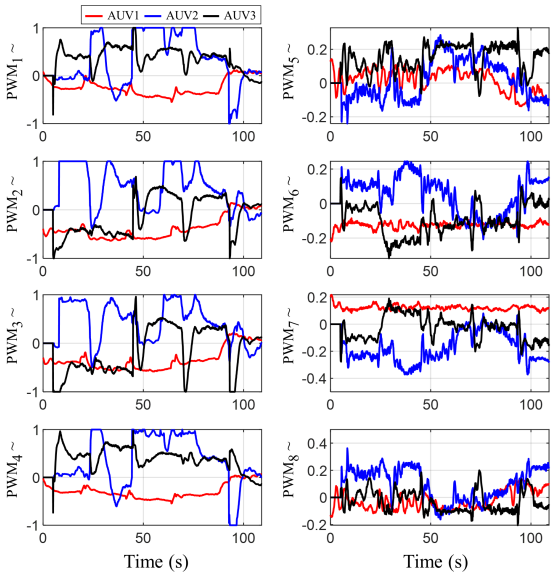

Fig. 13. Normalised PWM for eight thrusters of AUV1, AUV2, and AUV3

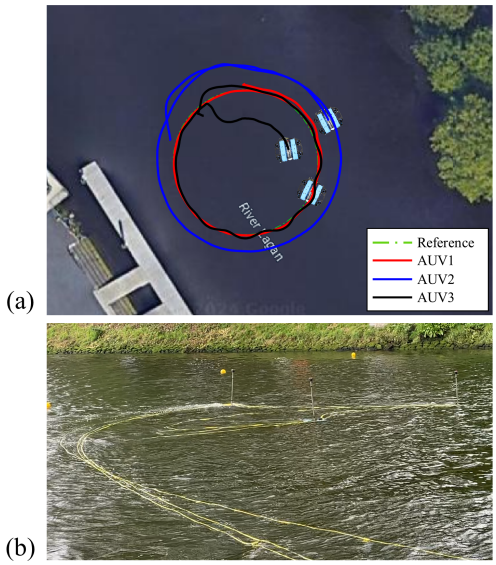

Fig. 14. (a) Overhead view of AUV trajectories. (b) Ground-level view of AUVs in Lagan.

was circular, defined by $\xi_{sr} = [4.3 + 5\cos(0.085t), 28.9 + 5\sin(0.085t), 0.5]^T$ (m). The AUVs transitioned between two formations during the tracking. These transitions were presented in Table II. All of the controller parameters were selected to be the same as in Section B-2.

The state tracking performance of three AUVs was plotted in Fig 15 with the initial poses as $\xi_{0,1} = [9.7.58.9, 0.46, 0, 0, 1.63]^T$, $\xi_{0,2} = [4.5, 25, 0.51, 0, 0, 0.6]^T$, and $\xi_{0,3} = [6.8, 26.7, 0.52, 0, 0, 0.74]^T$ and $\mathcal{V}_i = 0_{6\times1}, i \in \{1, 2, 3\}$ were the initial velocities. All agents closely followed the reference trajectory with different formations. Moreover, AUV3 effectively tracked AUV2 in its lateral direction, showcasing the flexibility of the proposed controllers in providing full spatial manoeuvrability and precise orientation control despite disturbances caused by tether cables and river currents. The optimal velocities and PWM control inputs of the three AUVs were plotted in Fig 16 and Fig 17. The control signals for all states, as well as the thrusters, reflected the dynamic efforts required to adapt to the water flow and the drag force of the tether cable.

5) Line Tracking and Formation Control of Multiple BlueRov2 at The River: In the last run, a more challenging scenario was set up by a long run against the river current. Five formations were formed along the predefined path. These transitions were presented in Table II. All of the controller parameters were selected to be the same as in Section B-2.

The state tracking performance of three AUVs was plotted in Fig 19 with the initial poses as $\xi_{0,1} = [15, 6.7, 0.5, 0, 0, 0]^T$, $\xi_{0,2} = [16.5, 7.5, 0.55, 0, 0, 0.3]^T$, and $\xi_{0,3} = [13.4, 5.3, 0.53, 0, 0, 0.1]^T$ and $\mathcal{V}_i = 0_{6\times1}, i \in \{1, 2, 3\}$ were the initial velocities. The x and y plots showed the deviations of AUV2 and AUV3 from AUV1, aligning with the

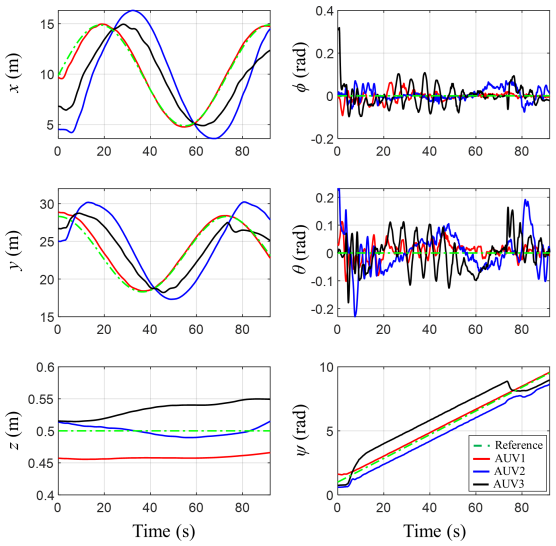

Fig. 15. Position and orientation tracking of AUV1, AUV2, and AUV3

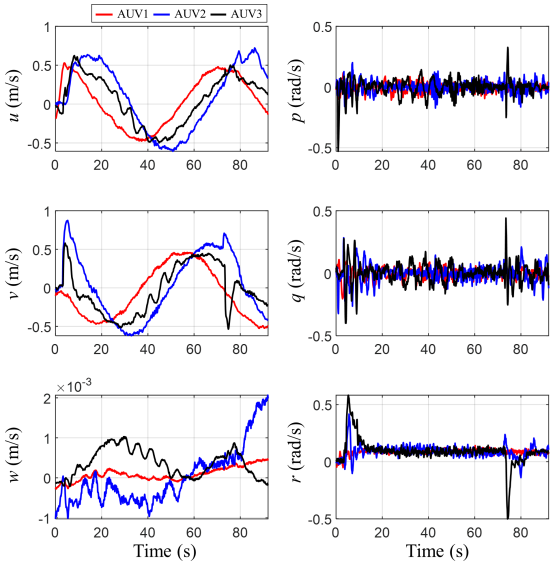

Fig. 16. Optimal control signals of AUV1, AUV2, and AUV3

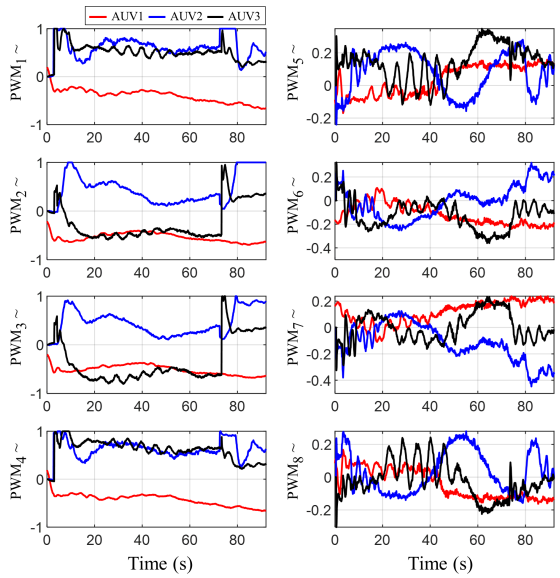

Fig. 17. Normalised PWM for eight thrusters of AUV1, AUV2, and AUV3

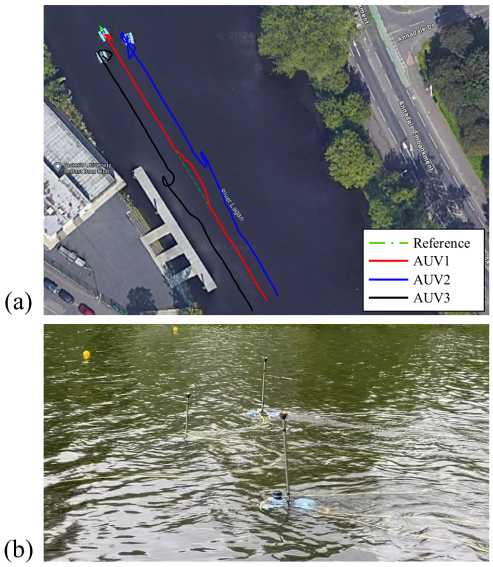

Fig. 18. (a) Overhead view of AUV trajectories. (b) Ground-level view of AUVs in Lagan.
(See Video 1 at https://youtu.be/9pJ6FKsCJBM)

strategic offsets required for the desired formations. All agents consistently tracked the reference trajectory despite the river flow. Notably, a significant error occurred in the y direction of AUV1 from 25 to 47 s because the tether cable from AUV2 was hanging over AUV1 while AUV2 was reaching a 3-m offset. This caused a large lateral force on AUV1. However, when the fourth formation was executed, the drag force disappeared as AUV2 reached its new position. The return of AUV1 to the defined path highlighted the robustness of the proposed controller. A similar situation occurred near the end of the run, around 80 s, when the controllers for AUV2 and AUV3 were shut down; the unstable state of these robots also caused a significant disturbance on AUV1. Nevertheless, AUV1 managed to return to the desired state by 97 s. A video demonstrating the experiment in detail is available online (Video 1). The optimal control signals for velocities and the PWM control inputs of the three AUVs were plotted in Fig 20 and Fig 21. Stable velocities and PWM control signals were observed for AUV1, while AUV2 and AUV3 exhibited large spikes due to the strategic offsets required for formation. Overall, the NMPC-Relax-CBF strategy effectively managed the control outputs, ensuring robust performance in the challenging river environment.

V. Conclusions

The experiment results aligned well with the SITL simulations and demonstrated the effectiveness of the distributed NMPC-Relaxed-CBF control strategy for coordinating multiple AUVs in both river and open sea environments. The independent Relax-CBF for each AUV enabled successful obstacle detection and avoidance, with the leader's strategy of

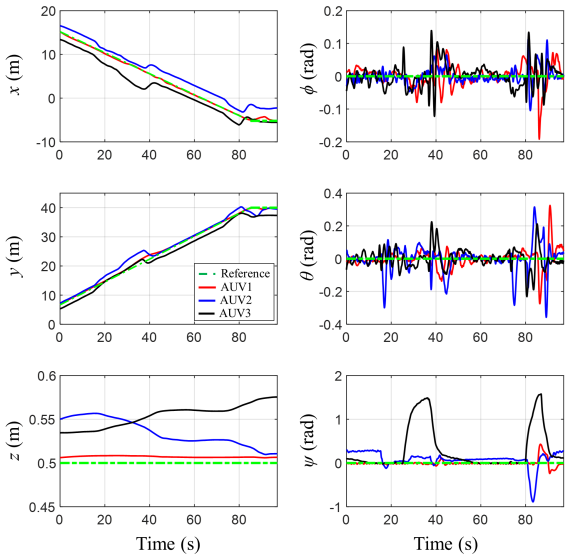

Fig. 19. Position and orientation tracking of AUV1, AUV2, and AUV3

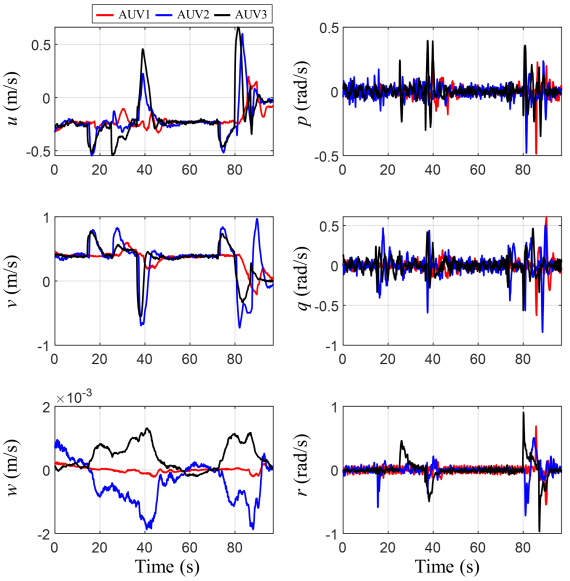

Fig. 20. Optimal control signals of AUV1, AUV2, and AUV3

broadcasting reference poses ensuring smooth follower trajectories. Despite occasional disturbances from tether cables, river currents, ocean waves, and tides, the AUVs maintained stable depths and dynamically adapted their velocities and control inputs to handle environmental influences. The experiment underscored the robustness and flexibility of the proposed control strategy, ensuring safe and coordinated multi-AUV operations.

For future work, a key area to examine is the localisation solution. Currently, we use a GPS mast for the global positioning of each ROV, which was chosen due to time and budget constraints. However, for full underwater manoeuvrability, alternative localisation mechanisms like Ultra-Short-Baseline and Doppler-Velocity-Logger should be considered. These systems may require modifications to the AUV platform for the necessary electrical and mechanical interfaces. Additionally, a

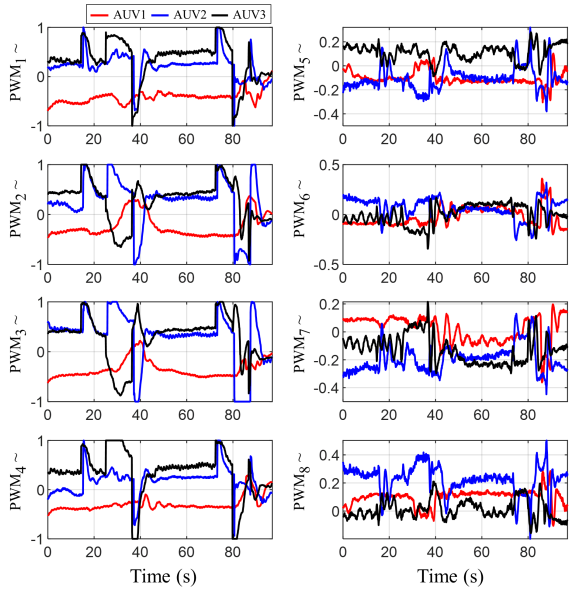

Fig. 21. Normalised PWM for eight thrusters of AUV1, AUV2, and AUV3

custom AUV controller AP could enable the dynamic NMPC to run locally on each ROV, paving the way for untethered, fully autonomous operation.

REFERENCES

[1] N. Kapetanović et al., "Marine robots mapping the present and the past: Unraveling the secrets of the deep," *Remote Sensing*, vol. 12, no. 23, p. 3902, 2020.

[2] C. L. Batchelor, A. Montelli, D. Ottesen, and J. Evans, "New insights into the formation of submarine glacial landforms from high-resolution Autonomous Underwater Vehicle data," *Geomorphology*, vol. 370, no. 107396, p. 107396, 2020.

[3] M. Woolsey, M. E. Clarke, and A. Woolsey, "Seafloor Imaging Lessons Learned from Over a Decade of Surveys with SeaBED AUVs," in *OCEANS 2022*, Hampton Roads, Hampton Roads, VA, USA, pp. 1-10, 2022.

[4] Y. Li, B. Li, W. Yu, S. Zhu, and X. Guan, "Cooperative Localization Based Multi-AUV Trajectory Planning for Target Approaching in Anchor-Free Environments," in *IEEE Transactions on Vehicular Technology*, vol. 71, no. 3, pp. 3092-3107, March 2022.

[5] D. Yu, H. Wang, X. Cao, Z. Wang, J. Ren, and K. Zhang, "Enhancing autonomous underwater vehicle decision making through intelligent task planning and behavior tree optimization," *Journal of Marine Science and Engineering*, vol. 12, no. 5, p. 791, 2024.

[6] X. Wang, J. Sun, Z. Wu, and Z. Li, "Robust integral of sign of error-based distributed flocking control of double-integrator multi-agent systems with a varying virtual leader," *International Journal of Robust and Nonlinear Control*, vol. 32, no. 1, pp. 286–303, 2022.

[7] Z. Wang, Y. Wang, Y. Sun, and H. Qin, "Fixed-time dynamic event-triggered three-dimensional formation control for multi-AUV system with disturbance observer," *Ocean Engineering*, vol. 308, no. 118165, p. 118165, 2024.

[8] H. Liu, Y. Wang and F. L. Lewis, "Robust Distributed Formation Controller Design for a Group of Unmanned Underwater Vehicles," *IEEE Transactions on Systems, Man, and Cybernetics: Systems*, vol. 51, no. 2, pp. 1215-1223, Feb. 2021.

[9] T. Yan, Z. Xu and S. X. Yang, "Distributed Robust Learning-Based Backstepping Control Aided With Neurodynamics for Consensus Formation Tracking of Underwater Vessels," *IEEE Transactions on Cybernetics*, vol. 54, no. 4, pp. 2434-2445, April 2024.

[10] W. Pang, D. Zhu and C. Sun, "Multi-AUV Formation Reconfiguration Obstacle Avoidance Algorithm Based on Affine Transformation and Improved Artificial Potential Field Under Ocean Currents Disturbance," *IEEE Transactions on Automation Science and Engineering*, vol. 21, no. 2, pp. 1469-1487, April 2024.

[11] X. Yan, D. Jiang, R. Miao, and Y. Li, "Formation control and obstacle avoidance algorithm of a multi-USV system based on virtual structure and artificial potential field," *Journal of Marine Science and Engineering*, vol. 9, no. 2, p. 161, 2021.
[12] M. Van, Y. Sun, S. Mcllvanna, M.-N. Nguyen, F. Zocco and Z. Liu, "Control of Multiple AUV Systems With Input Saturations Using Distributed Fixed-Time Consensus Fuzzy Control," *IEEE Transactions on Fuzzy Systems*, vol. 32, no. 5, pp. 3142-3153, May 2024.
[13] Z. Gao and G. Guo, "Fixed-Time Leader-Follower Formation Control of Autonomous Underwater Vehicles With Event-Triggered Intermittent Communications," *IEEE Access*, vol. 6, pp. 27902-27911, 2018.
[14] H. Li, P. Xie and W. Yan, "Receding Horizon Formation Tracking Control of Constrained Underactuated Autonomous Underwater Vehicles," *IEEE Transactions on Industrial Electronics*, vol. 64, no. 6, pp. 5004-5013, June 2017.
[15] Y. Yang, Y. Xiao, and T. Li, "A survey of autonomous underwater vehicle formation: Performance, formation control, and communication capability," *IEEE Communications Surveys & Tutorials*, vol. 23, no. 2, pp. 815–841, 2021.
[16] T. Yan, Z. Xu, and S. X. Yang, "Consensus formation control for multiple AUV systems using distributed bioinspired sliding mode control," *IEEE Transactions on Intelligent Vehicles*, vol. 8, no. 2, pp. 1081–1092, Feb. 2023.
[17] G. Xia, Y. Zhang, W. Zhang, X. Chen, and H. Yang, "Dual closed-loop robust adaptive fast integral terminal sliding mode formation finite-time control for multi-underactuated AUV system in three dimensional space," *Ocean Engineering*, vol. 233, 2021.
[18] M. Van, V. T. Do, M. O. Khyam, and X. P. Do, "Tracking control of uncertain surface vessels with global finite-time convergence," *Ocean Engineering*, vol. 241, 2021.
[19] S. Li and X. Wang, "Finite-time consensus and collision avoidance control algorithms for multiple AUVs," *Automatica*, vol. 49, no. 11, pp. 3359–3367, 2013.
[20] B. Chen, J. Hu, Y. Zhao, and B. K. Ghosh, "Finite time velocity free observer based consensus tracking for heterogeneous uncertain AUVs via adaptive sliding mode control," *Ocean Engineering*, vol. 237, 2021.
[21] Z. Gao and G. Guo, "Fixed-time leader-follower formation control of autonomous underwater vehicles with event-triggered intermittent communications," *IEEE Access*, vol. 6, pp. 27902–27911, 2018.
[22] Y. Su, H. Xue, H. Liang, and D. Chen, "Singularity avoidance adaptive output-feedback fixed-time consensus control for multiple autonomous underwater vehicles subject to nonlinearities," *International Journal of Robust and Nonlinear Control*, vol. 32, no. 7, pp. 4401–4421, 2022.
[23] Z. Wang, L. Zhang, and Z. Zhu, "Game-based distributed optimal formation tracking control of underactuated AUVs based on reinforcement learning," *Ocean Engineering*, vol. 287, no. 115879, p. 115879, 2023.
[24] Y. Zhang, T. Zhang, Y. Li, and Y. Zhuang, "Tracking control of AUV via novel soft actor-critic and suboptimal demonstrations," *Ocean Engineering*, vol. 293, no. 116540, p. 116540, 2024.
[25] C. Wu, H. R. Karimi, L. Shan, and Y. Dai, "Data-driven iterative learning cooperative trajectory tracking control for multiple autonomous underwater vehicles with input saturation constraints," *Journal of Field Robotics*, 2024.
[26] S. Heshmati, G. C. Karras, P. Marantos, and K. J. Kyriakopoulos, "A Robust Predictive Control Approach for Underwater Robotic Vehicles," *IEEE Transactions on Control Systems and Technology*, vol. 28, no. 6, pp. 2352–2363, Nov. 2020.
[27] Z. Yan, P. Gong, W. Zhang, and W. Wu, "Model predictive control of autonomous underwater vehicles for trajectory tracking with external disturbances," *Ocean Engineering*, vol. 217, pp. 107884–107884, Dec. 2020.
[28] C. Shen, Y. Shi, and B. Buckham, "Integrated Path Planning and Tracking Control of an AUV: A Unified Receding Horizon Optimization Approach," *IEEE-ASME Transactions on Mechatronics*, vol. 22, no. 3, pp. 1163–1173, 2017.
[29] H. Li, P. Xie, and W. Yan, "Receding horizon formation tracking control of constrained underactuated autonomous underwater vehicles," *IEEE Transactions on Industrial Electronics*, vol. 64, no. 6, pp. 5004–5013, Jun. 2017.
[30] H. Wei, C. Shen, and Y. Shi, "Distributed Lyapunov-Based Model Predictive Formation Tracking Control for Autonomous Underwater Vehicles Subject to Disturbances," *IEEE Transactions on Systems, Man, and Cybernetics*, vol. 51, no. 8, pp. 5198–5208, 2021.
[31] A. D. Ames et al., "Control Barrier Functions: Theory and Applications," *18th European Control Conference (ECC)*, Naples, Italy, pp. 3420-3431, 2019.
[32] M. -N. Nguyen et al., "Model-Free Safety Critical Model Predictive Control for Mobile Robot in Dynamic Environments," in *IEEE Transactions on Intelligent Vehicles*, doi: 10.1109/TIV.2024.3389111.
[33] NM. Nhat, S. McIlvanna, Y. Sun, Y. Jin, and M. Van, "Enhancing Mobile Robot Navigation Safety and Efficiency through NMPC with Relaxed CBF in Dynamic Environments," in *Proceedings of the IEEE International Conference on Automation Science and Engineering*, 2024, https://arxiv.org/abs/2211.11348.
[34] J. Zeng, Z. Li, and K. Sreenath, "Enhancing Feasibility and Safety of Nonlinear Model Predictive Control with Discrete-Time Control Barrier Functions," *IEEE Conference on Decision and Control*, Dec. 2021.
[35] R. Kot, "Review of Obstacle Detection Systems for Collision Avoidance of Autonomous Underwater Vehicles Tested in a Real Environment," *Electronics*, vol. 11, no. 21, p. 3615, Nov. 2022.
[36] Bock, H.G. and Plitt, K.J, "A multiple shooting algorithm for direct solution of optimal control problems," *Proceedings 9th IFAC World Congress Budapest*, Pergamon Press, pp. 243-247, 1984.
[37] L. Magni, D. Martino. Raimondo, and F. Allgower, *Nonlinear Model Predictive Control: Towards New Challenging Applications*. Berlin, Heidelberg: Springer Berlin Heidelberg, 2009.
[38] J. B. Rawlings and M. J. Risbeck, "Model predictive control with discrete actuators: Theory and application," *Automatica*, vol. 78, pp. 258-265, 2017.
[39] L. Grüne and J. Pannek, *Nonlinear Model Predictive Control*. Berlin, Germany: Springer, 2017.

VI. Biography Section

Minh-Nhat Nguyen is currently working toward the Ph.D. degree in robotics and intelligent control with the School of Electronics, Electrical Engineering and Computer Science, Queen's University of Belfast, Belfast, U.K.

Stephen McIlvanna is currently working toward the Ph.D. degree in robotics and intelligent control with the School of Electronics, Electrical Engineering and Computer Science, Queen's University of Belfast, Belfast, U.K.

Jack Close is currently working toward the Ph.D. degree in robotics and intelligent control with the School of Electronics, Electrical Engineering and Computer Science, Queen's University of Belfast, Belfast, U.K.

Mien Van is a Senior Lecturer (Associate Professor) in Robotics and Control Engineering with the School of Electronics, Electrical Engineering and Computer Science, Queen's University Belfast, United Kingdom. He has authored and co-authored for over 65 journals and conference papers and some are published in prestigious journals such as IEEE Transactions on Fuzzy Systems, IEEE/ASME Transactions on Mechatronics, IEEE Transactions on Industrial Informatics, IEEE Transactions on Cybernetics, etc. His current research interests include manufacturing robotics, robot control, robot-vision systems, fault diagnosis and fault tolerant, machine learning, and sensing and perception.

Charalampos C. Tsimenidis (Senior Member, IEEE) received a PhD degree in communications and signal processing from Newcastle University in 2002. He is currently a Professor of digital innovation at Nottingham Trent University. He has published over 230 conference and journal papers, successfully supervised three M.Phil. and 50 PhD students and made contributions in the area of digital communications to several U.K. and European-funded research projects. His main research interests include digital communications and signal processing with specialisation in massive multiple-input multiple-output systems, adaptive filter, and demodulation algorithms, error control and network coding for radio frequency, and underwater acoustic channels. He is a member of the IET.